

PAPER • OPEN ACCESS

# Modeling of plasma beta effects on the island divertor transport in the standard configuration of W7-X


To cite this article: S. Xu *et al* 2023 *Nucl. Fusion* **63** 066005

View the [article online](#) for updates and enhancements.

You may also like

- [Gyrokinetic analysis of microinstabilities in a stellarator reactor](#)  
Alexander Kendl
- [Equilibrium effects on the structure of island divertor and its impact on the divertor heat flux distribution in Wendelstein 7-X](#)  
S. Zhou, Y. Liang, A. Knieps et al.
- [Finite beta effects on MHD equilibria and energetic ion losses in a rippled tokamak](#)  
M. Bunno, Y. Nakamura, Y. Suzuki et al.

# Modeling of plasma beta effects on the island divertor transport in the standard configuration of W7-X

S. Xu<sup>1,\*</sup> , Y. Liang<sup>1,2,6,\*</sup> , A. Knieps<sup>1</sup> , S. Zhou<sup>2</sup> , Y. Feng<sup>3</sup> , D. Reiter<sup>4</sup> , Y. Suzuki<sup>5</sup> , M. Jia<sup>6</sup> , J. Geiger<sup>3</sup> , F. Reimold<sup>3</sup> , R. König<sup>3</sup> , A. Dinklage<sup>3</sup> , D. Harting<sup>1</sup> , Y. Luo<sup>1</sup> , P. Drews<sup>1</sup> , M. Jakubowski<sup>3</sup> , Y. Gao<sup>3</sup> , E. Pasch<sup>3</sup> , A. Pandey<sup>3</sup> , A. Langenberg<sup>3</sup> , N. Pablant<sup>7</sup> , S. Brezinsek<sup>1</sup> , E. Wang<sup>1</sup> , S. Liu<sup>6</sup> , H.M. Xiang<sup>1</sup> , O. Neubauer<sup>1</sup> , J. Huang<sup>1,2</sup> , J. Cai<sup>1,6</sup> , J. Yang<sup>1,2</sup> , J. Liu<sup>1,6</sup> , L. Liao<sup>1,6</sup> , Y.C. Gao<sup>1</sup>  and the W7-X Team<sup>a</sup>

<sup>1</sup> Forschungszentrum Jülich GmbH, Institut für Energie- und Klimaforschung-Plasmaphysik, Partner of the Trilateral Euregio Cluster (TEC), 52425 Jülich, Germany

<sup>2</sup> International Joint Research Laboratory of Magnetic Confinement Fusion and Plasma Physics, State Key Laboratory of Advanced Electromagnetic Engineering and Technology, School of Electrical and Electronic Engineering, Huazhong University of Science and Technology, Wuhan 430074, China

<sup>3</sup> Max-Planck-Institute für Plasmaphysik, 17491 Greifswald/85748 Garching, Germany

<sup>4</sup> Institute for Laser and Plasma Physics, Heinrich-Heine-University, D-40225 Düsseldorf, Germany

<sup>5</sup> Graduate School of Advanced Science and Engineering, Hiroshima University, 739-8527 Higashi-Hiroshima, Japan

<sup>6</sup> Institute of Plasma Physics, Chinese Academy of Sciences, Hefei 230031, China

<sup>7</sup> Princeton Plasma Physics Laboratory, Princeton, NJ 08540, United States of America

E-mail: [s.xu@fz-juelich.de](mailto:s.xu@fz-juelich.de) and [y.liang@fz-juelich.de](mailto:y.liang@fz-juelich.de)

Received 23 September 2022, revised 22 March 2023

Accepted for publication 27 March 2023

Published 11 April 2023



## Abstract

The influence of plasma beta effects on the edge plasma transport in the Wendelstein 7-X standard configuration is studied systematically by using EMC3-EIRENE combined with a 3D equilibrium code named HINT. The magnetic topology changes induced by plasma beta effects are significantly reflected in plasma transport behaviors and heat flux patterns on divertor targets. After validating the modeling strategy by comparisons with experimental data, the extended simulations for high performance plasmas show that the threshold separatrix density for accessing the power detachment is reduced in higher beta plasmas. Compared with the vacuum field case, the impurity radiation distributions with finite beta effects are modified in the magnetic island region. The divertor heat flux is distributed more evenly along the toroidal direction on the strike line at the vertical target. The strike line on the horizontal target moves towards the pumping gap with an increase in the plasma beta. In addition, the different pressure profiles with the same central beta also result in a modified heat flux pattern on the divertor targets.

<sup>a</sup> See Sunn Pedersen *et al* 2022 (<https://doi.org/10.1088/1741-4326/ac2cf5>) for the W7-X Team.

\* Authors to whom any correspondence should be addressed.



Original Content from this work may be used under the terms of the [Creative Commons Attribution 4.0 licence](https://creativecommons.org/licenses/by/4.0/). Any further distribution of this work must maintain attribution to the author(s) and the title of the work, journal citation and DOI.

Keywords: EMC3-EIRENE, beta effect, magnetic topology, edge plasma transport, island divertor

(Some figures may appear in colour only in the online journal)

## 1. Introduction

As an advanced fusion stellarator device, Wendelstein 7-X (W7-X) has optimized magnetic field designed to overcome major issues in the neoclassical transport, fast particle confinement, as well as magnetohydrodynamic (MHD) equilibrium and stability, especially in high beta plasmas [1–6]. One of the W7-X operation purposes is demonstrating steady-state high-performance plasmas with a volume-averaged beta of up to 5%. In the last campaign (OP1.2b), the plasma performance of W7-X has significantly improved after utilizing island divertor configurations. The plasma has achieved a good performance with a volume-averaged beta of up to 1.2%, and a plasma beta of up to 3.5% at the magnetic axis [7]. It can be foreseen that the plasma beta will be even higher in the next campaign (OP2) benefitting from device upgrades. At these levels, MHD currents in the plasma may be strong enough to modify the vacuum magnetic field, thus resulting in the magnetic topology changes [8–12]. Previous studies have also showed that the divertor plasma operation is highly dependent on the magnetic topology [13–24]. Therefore, the study on edge plasma transport with finite beta effects is an essential topic for high-performance plasmas in future W7-X experiments.

This work systematically presents the influence of the beta effect induced magnetic topology changes on the edge plasma transport and divertor heat loads in standard configurations on W7-X by using EMC3-EIRENE combined with the HINT code [25–30]. Hereinto, HINT evolves the resistive MHD equations in time, utilizing resistive and viscous terms to dissipate energy from the magnetic field and plasma flow, thus leading to a relaxation towards a steady-state 3D equilibrium. It can provide the magnetic field distributions to the 3D self-consistent edge plasma code EMC3-EIRENE, which consists of the fluid edge plasma transport code EMC3 and the kinetic neutral particle transport code EIRENE. EMC3 solves a set of Braginskii fluid equations formulated in a Fokker–Planck scheme by using the Monte-Carlo method, while the EIRENE code is for multi-species Boltzmann equations with chemical processes, based on conventional Monte-Carlo particle transport algorithms [31]. EMC3-EIRENE have already shown their powerful abilities in previous simulated and even predicted studies performed on many stellarator devices, such as Large Helical Device [32–34], W7-AS [35–38] and W7-X [39–46]. Most of these works are not taking into account the plasma beta effect. In this study, the grid generation code for EMC3-EIRENE on W7-X is improved to be capable of using HINT results directly. Based on this, we will first validate the modeling strategy by comparing modeling results with the experimental data from the last campaign (OP1.2) of W7-X, and then extend the studies to investigate finite plasma beta

effects on the power dissipation in the standard configuration under an OP2 candidate heating power condition with the island divertor.

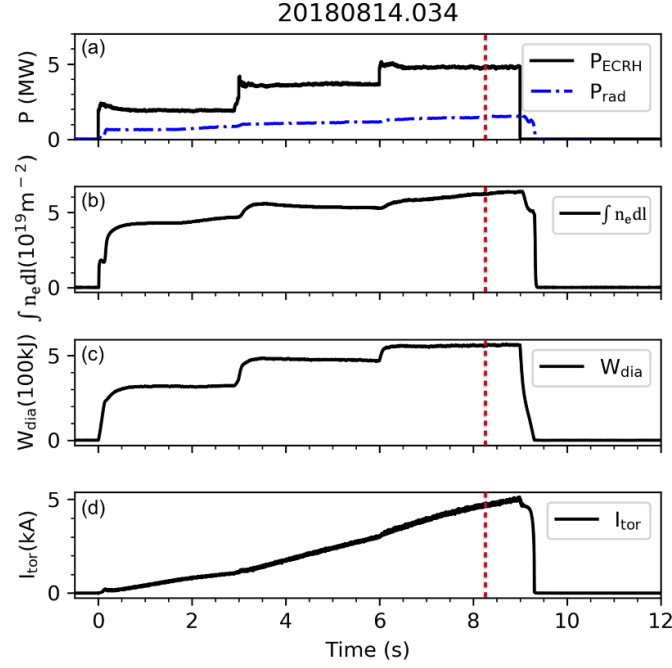
The outline of this paper is as follows. Based on an experimental discharge from the last campaign on W7-X, a comparison work between modeling and diagnostics will be presented to show the validation of the modeling strategy in section 2. The section 3 will pay attention to the influence of plasma beta effects on the power dissipation in high heating power scenarios with the standard configuration. Three factors will be discussed in detail, including the plasma beta strength, the plasma pressure profile and the toroidal plasma current amplitude. Finally, the conclusions are summarized and discussed in section 4.

## 2. Validation of the modeling strategy

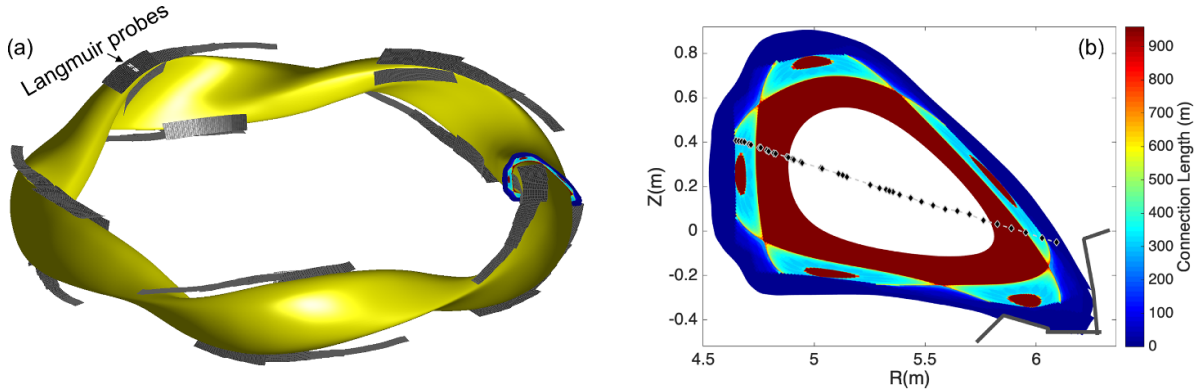
### 2.1. Experimental set-up

As the most advanced stellarator in the current world, W7-X is designed to demonstrate high heating power (10 MW) steady-state operations with reactor-relevant plasma parameters at pulse-length up to 30 min. The plasma volume is about 30 m<sup>3</sup> with the major radius 5.0 m and minor radius 0.50 m. The device has five identical modules with an up-down symmetry between the two halves of each module. The flexible magnetic configurations generated by superconducting coils are characterized with the edge rotational transform  $\iota_a = n/m$ , where  $n$  and  $m$  are the toroidal and poloidal mode number, respectively [47]. This work focuses on the standard configuration with  $\iota_a = 5/5$ , in which five magnetic island chains are independent from each other.

To validate the modeling strategy, a representative standard configuration shot (ID #20180814034) with available experimental data from various diagnostics is employed in the following modeling and analysis. The time evolution of main hydrogen plasma parameters in the selected shot is shown in figure 1. At the studied moment ( $t = 8.25$  s) marked by the vertical dashed line, an electron-cyclotron-resonance-heating power of  $\sim 5$  MW is applied. The total radiation power measured by the bolometer is  $\sim 2$  MW [48, 49]. The toroidal plasma current dominated by the bootstrap current is  $\sim 4.66$  kA, which is measured by the in-vessel Rogowski coil encircling the plasma volume. The positions of diagnostic systems used in this work are indicated in figure 2, including the Thomson scattering (TS) system and divertor Langmuir probes [50, 51]. Figure 2(b) shows the specific measurement points of the TS system at its cross-section. In addition, the infrared thermography cameras are able to provide the heat flux distribution on divertor targets [52, 53].



**Figure 1.** Time evolution of the W7-X shot #20180814034, including (a) the heating power and the radiation power, (b) the line-integral electron density, (c) the diamagnetic energy and (d) the toroidal plasma current. The dashed line corresponds to the modeling moment.



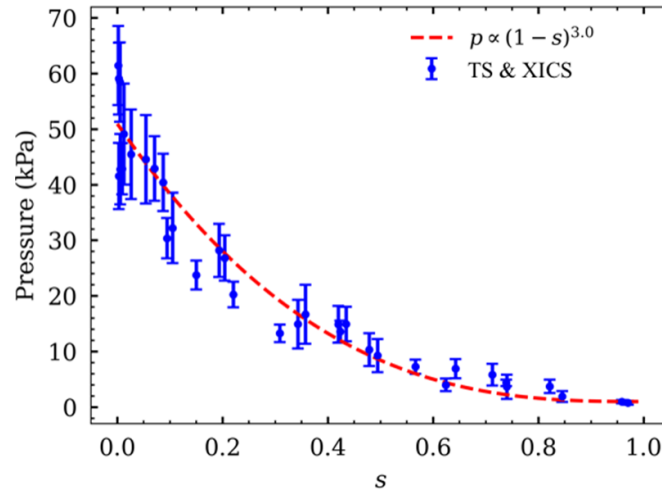
**Figure 2.** Sketch of diagnostic positions and plasma shape taken from the 3D equilibrium reconstruction at 8.25 s in the selected discharge #20180814034. The white points in (a) indicate the positions of the divertor Langmuir probes. The poloidal plane with connection length plot in (a) corresponds to the toroidal location of the TS measurements. The black points in (b) represent the measurement positions of the TS system.

## 2.2. Modeling set-up

The modeling strategy in this work is using the synergy of HINT and EMC3-EIRENE. As mentioned above, HINT calculations provide the 3D magnetic equilibrium with beta effects to the EMC3-EIRENE code. Some inputs are necessary to HINT calculations including the vacuum magnetic field, the plasma pressure profile, and the toroidal plasma current. Here, the plasma pressure profile is utilized by the form  $p \propto (1-s)^\alpha$ , where  $s$  is the normalized toroidal flux. Such form has an acceptable fit to experimental measurements derived from TS system and X-ray Imaging Crystal Spectrometer [54]. A good agreement can be accessed in the selected discharge if assuming  $\alpha = 3$  as shown in figure 3. The plasma beta at the magnetic axis, so called the central beta, is  $\sim 2.0\%$  based on the measurements, where the beta equals to  $p/(B^2/2\mu_0)$ .

The grid generation for EMC3-EIRENE on W7-X is improved to be capable of using HINT results directly. To reduce computational efforts, the 3D calculation grids only cover a toroidal segment of  $36^\circ$  based on the configuration symmetry, that is the five-fold periodicity and the up-down stellarator symmetry. The toroidal position at  $\varphi = 0^\circ$  and  $\varphi = 36^\circ$  are defined at the bean-shaped and triangular cross-sections, respectively.

After completing the grid generation, some boundary conditions provided from experimental measurements are necessary to solve the transport equations in EMC3-EIRENE. The input power across the innermost grid surface is  $\sim 5$  MW obtained from the experiment. Similar to the previous EMC3-EIRENE work on W7-X [44], the simulation domain is optimized to cover the main radiation region due to the power



**Figure 3.** Comparisons of the experimental radial pressure profile and the input pressure profile used in the HINT calculation.

balance. The plasma density at the separatrix is set to  $1.5 \times 10^{19} \text{ m}^{-3}$ ,  $2.5 \times 10^{19} \text{ m}^{-3}$ ,  $3.0 \times 10^{19} \text{ m}^{-3}$  or  $4.5 \times 10^{19} \text{ m}^{-3}$ , based on the TS data with the error bar. The uniform anomalous cross-field transport coefficients for particles  $D$  and energy  $\chi$  are firstly determined by fitting the electron density and temperature profiles measured by TS measurements. For sensitivity studies shown in the following simulations, the diffusivity  $D$  for both hydrogen and the impurity are assumed as  $0.50 \text{ m}^2 \text{ s}^{-1}$  or  $1.0 \text{ m}^2 \text{ s}^{-1}$ . The electron and ion thermal conductivities are equally set to  $\chi = 0.75 \text{ m}^2 \text{ s}^{-1}$  or  $1.5 \text{ m}^2 \text{ s}^{-1}$ . The global particle balance is self-sustained by assuming 100% recycling on plasma-facing components without external particle sources. External particle sources can be neglected as they are much smaller than the recycling flux in experiments.

About the impurity modeling, carbon particles released from divertor and baffle targets are assumed to be the only impurity radiator. The ionized carbon species are simulated by using a fluid model with a classical convection and an anomalous diffusion process [55]. The total carbon influx is controlled either by an effective sputtering coefficient or by the radiation power in the entire computation domain. Here, the sputtering coefficient is the ratio between carbon yield and the recycling flux. It is assumed as 0.04 in the following simulations similar to the previous studies [44, 45]. The carbon radiation power is set to  $\sim 2 \text{ MW}$  according to the experiments.

The atomic and molecular physics model employed in EIRENE for this study incorporates the most essential reaction processes that occur in the island divertor region. It is similar to the so-called Kotov model [56]. The specific reactions are presented in table 1. So far, there is no significant volume recombination observed on W7-X [45]. Therefore, the volume recombination process is neglected in the following simulations of this work.

### 2.3. Comparisons between modeling results and the experimental data

The magnetic topology with the HINT equilibrium is simulated in the EMC3-EIRENE grid by tracing magnetic field

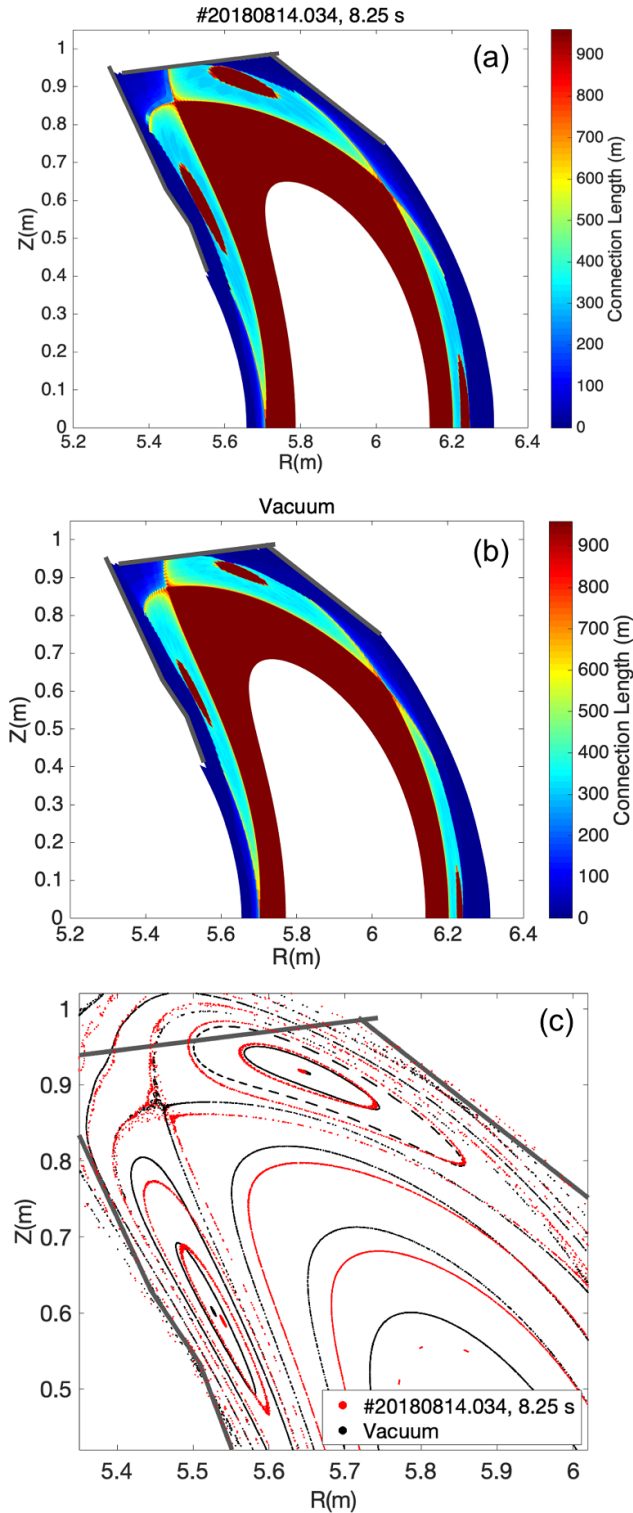
**Table 1.** The atomic and molecular processes for hydrogen used in the following EIRENE simulations.

Reaction	Note
$\text{H} + \text{e} \rightarrow \text{H}^+ + 2\text{e}$	Multistep ionization
$\text{H} + \text{H}^+ \rightarrow \text{H}^+ + \text{H}$	Charge-exchange
$\text{H}_2 + \text{e} \rightarrow \text{H}_2^+ + 2\text{e}$	Non-dissociative ionization
$\text{H}_2 + \text{e} \rightarrow 2\text{H} + \text{e}$	Dissociation
$\text{H}_2 + \text{e} \rightarrow \text{H} + \text{H}^+ + 2\text{e}$	Dissociative ionization
$\text{H}_2^+ + \text{e} \rightarrow \text{H} + \text{H}^+ + \text{e}$	Dissociative excitation
$\text{H}_2^+ + \text{e} \rightarrow 2\text{H}^+ + 2\text{e}$	Dissociative ionization
$\text{H}_2^+ + \text{e} \rightarrow 2\text{H}$	Dissociative recombination
$\text{H}_2 + \text{H}^+ \rightarrow \text{H}_2 + \text{H}^+$	Elastic collision

lines as shown in figure 4. The figure only shows the top half at the bean shape cross-section due to the up-down symmetry. Compared with the vacuum field case, it demonstrates that not only the magnetic island width changes, but also the connection length distribution of field lines in magnetic islands is modified due to the beta effect and the toroidal plasma current.

According to the boundary conditions discussed in the previous sub-section, the 3D edge plasma properties are simulated by the EMC3-EIRENE code. Figure 5 indicates the electron temperature and the electron density profiles compared with the TS data along with the measurement line as shown in figure 2(b). The modeling results agree with the TS data within the range of experimental and simulated uncertainties. Currently, the TS system on W7-X is not a specific diagnostic for the edge plasma, as evidenced by the lack of complete plasma coverage on the inboard side and the insufficient channel resolution on the outboard side. It seems that the precise free input parameters of the EMC3-EIRENE modeling are not easy to be determined by TS data only. Figure 6 presents an example of the simulated 2D electron density and electron temperature distributions in the modeling case 2. The structure of the magnetic island is clearly reflected at the edge plasma, because of much stronger parallel field transport compared with the cross-field diffusion.





**Figure 4.** The connection length of magnetic field lines using (a) HINT results and (b) the vacuum field. Figure (c) shows the Poincaré plot of the magnetic field lines for the studied two cases. The HINT case is represented by red color, while the vacuum field scenario is represented by black color.

To further validate the modeling strategy, the comparisons between simulations and experiments at the downstream position are also illustrated in the following. Figure 7 shows 1D profiles of the heat flux on the horizontal target at

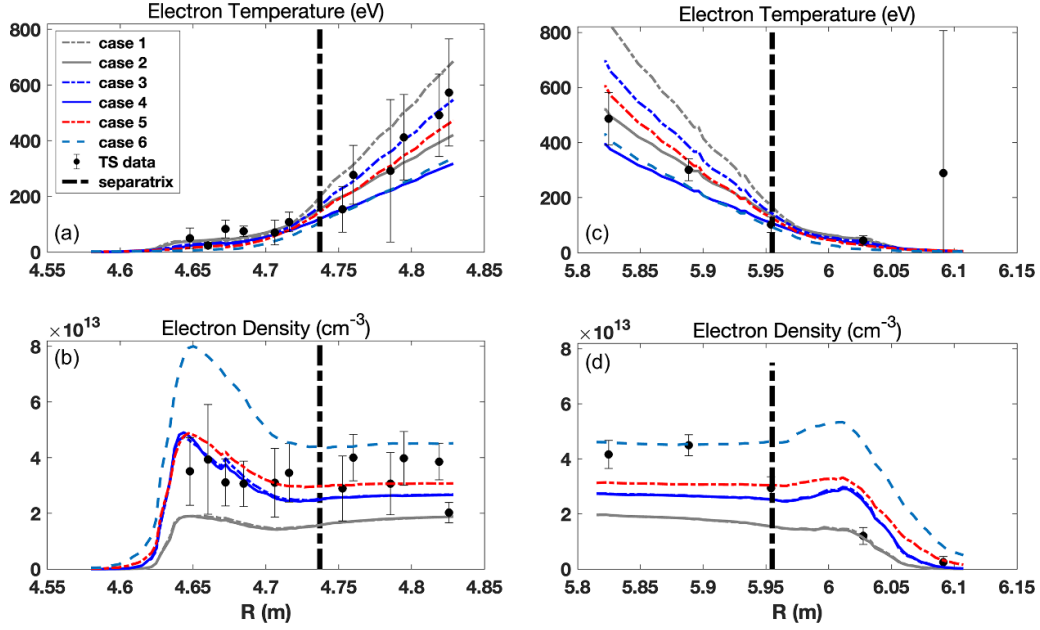
stellarator-symmetric toroidal locations with divertor Langmuir probes. The dashed profiles in the background are the experimental data measured by infrared cameras from different divertor modules. The reason why they have many discrepancies, including the profile width and peak flux value, has not been cleared yet. The possible reasons should be error fields and drift effects, which are not involved in the EMC3-EIRENE model now. Due to the perfect stellarator-symmetry used in the modeling, the averaged experimental heat flux from different divertor modules shown as the black solid curve provides a reference option to do the comparison. From this figure, the cases 2 and 3 show better quantitative agreements with the averaged experimental heat flux, which also have reasonable agreements with TS data. Furthermore, the 3D divertor heat flux pattern between the modeling and infrared camera data are quite similar as shown in figures 8 and 9. The strike line location between them also shows a good agreement. However, many quantitative discrepancies still can be found in detail comparisons. For instance, the simulated results for the high iota tail target are lower than the experimental values, and the simulated peak heat flux on the vertical target also falls short of the experimental values. These imply that the quantitative agreement can only be established at specific locations.

Figure 10 displays the comparison of the parallel particle flux between the divertor Langmuir probe data and the modeling results in the case 2 and 3. Here, only case 2 has a good agreement with the divertor Langmuir probe data, which indicates that the experimental data from multiple diagnostics are needed to improve input free parameters of EMC3-EIRENE modeling, because of the complex 3D effects in stellarator plasmas. In addition, the agreement between the modeling and experimental data means that the modeling strategy is feasible in the edge plasma transport study.

### 3. EMC3-EIRENE modeling in the high heating power scenario by utilizing the HINT equilibrium with plasma beta effects

One of the key challenges for magnetic confinement fusion devices on the path to a reactor is reducing damage to plasma-facing components from particles in the edge plasma during long-pulse, high-performance discharges. The detachment regime is an effective approach for dissipating most of energy before it reaches divertor targets. In the last campaign, power detachment plasmas have already achieved on W7-X through volume radiation at the plasma edge [44, 45, 49, 57, 58]. In this section, the EMC3-EIRENE code combined with HINT is employed to systematically study the plasma beta and toroidal current effects on power dissipation in the standard configuration with the island divertor. Three factors will be discussed in detail: the plasma beta strength, the plasma pressure profile and the toroidal plasma current amplitude.

Same as in present experiments, hydrogen plasmas are assumed in the following modeling. The input power is fixed at 10 MW, which is a candidate heating power value for OP2. Similar to the better case in the previous section, the cross-field transport coefficients for particles  $D$  and energy  $\chi$  are set



**Figure 5.** The radial experimental and simulated profiles of the electron temperature and the electron density at TS measurement positions as shown in figure 2. Figures (a) and (b) correspond to the inboard position. Figures (c) and (d) show the comparisons at the outboard position. The case number in the legend corresponds to the input parameter as shown in table 2.

**Table 2.** The input separatrix density and cross-field transport coefficients in different modeling cases.

Case	$n_{es}$ ( $m^{-3}$ )	$D$ ( $m^2 s^{-1}$ )	$\chi$ ( $m^2 s^{-1}$ )
Case 1	$1.5 \times 10^{19}$	0.5	0.75
Case 2	$1.5 \times 10^{19}$	0.5	1.5
Case 3	$2.5 \times 10^{19}$	0.5	0.75
Case 4	$2.5 \times 10^{19}$	0.5	1.5
Case 5	$3.0 \times 10^{19}$	1.0	0.75
Case 6	$4.5 \times 10^{19}$	1.0	0.75

to  $0.50 m^2 s^{-1}$  and  $1.5 m^2 s^{-1}$ , respectively. Carbon sputtered from divertor and baffle targets is the only representative impurity species. The sputtering coefficient is set to 0.04, which can be regarded as a boundary condition for carbon sources. The radiation power is calculated according to the carbon sources based on the ADAS database.

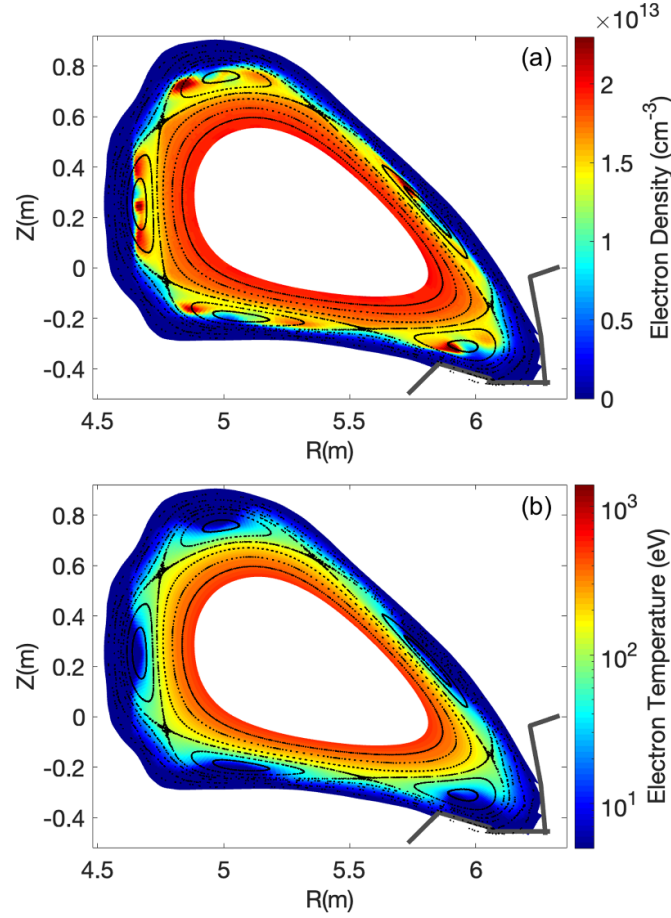
It should be mentioned that the following EMC3-EIRENE modeling are only qualitative studies focusing on magnetic topology changes induced by plasma beta effects. The simulated plasma density and electron profiles are not self-consistent with the pressure profile in HINT calculations. The reason is that there are no experiments to be used as references so far. Obtaining a self-consistent pressure profile is difficult, particularly in the plasma core region, because EMC3-EIRENE calculations focus primarily on the edge plasma. This is also why the density scan is used in the following studies.

### 3.1. Plasma beta strength

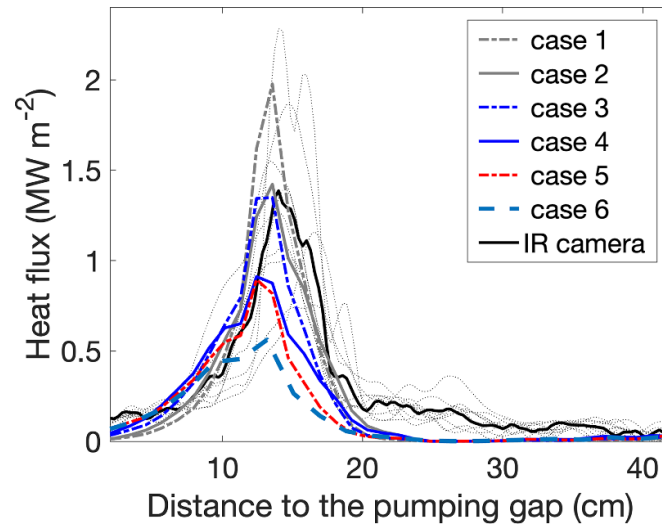
This subsection focuses on the influence of the plasma beta strength. In the modeling, the plasma pressure profiles used

in HINT are assumed same with the last section based on experiments, that is  $p \propto (1-s)^3$ . Three scenarios will be discussed, including the vacuum field, plasma beta at the magnetic axis ( $\beta_{axis}$ ) of 3% and 5%, which correspond to a volume-averaged beta ( $\beta_{vol}$ ) of  $\sim 0.75\%$  and  $\sim 1.25\%$ , respectively. The connection length distribution of magnetic field lines at the bean shape cross-section without the toroidal plasma current is shown in figure 11. Combined with figure 4(b), the magnetic island structure is modified by plasma beta effects, especially in the magnetic island phase and the island width. The arrows in the figure 11(b) mark the magnetic island core shifts in the poloidal direction. The volume of the plasma core region also shrinks.

The impurity radiation distributions with finite beta effects are simulated by EMC3-EIRENE using density scan. Figure 12 illustrates the changes of impurity radiation distributions with an increase in the plasma separatrix density at the bean shape cross-section. The  $f_{rad}$  parameter is the radiation fraction of the total input power. From the figure, it can be seen that the radiation region moves towards the core as the plasma density increases. Not only is the radiation distribution significantly modified, but its amplitude is also altered as a result of changes in the magnetic topology induced by plasma beta effects. Compared figure 12(a) with figure 12(b), the total radiation power is quite different with same separatrix density between the vacuum field case and the high beta case. Meanwhile, the separatrix density has also a marked difference in these two cases if the radiation powers are almost same as indicated in figures 12(c) and (d). In addition, the long connection length region along the separatrix touches the vertical target in the high beta case, thus resulting a higher radiation power area near the vertical target at the bean shape cross-section.



**Figure 6.** The poloidal cross-sections of the (a) electron density and (b) electron temperature simulated by EMC3-EIRENE at the same toroidal position with the TS measurement. The black points depict the Poincaré plot of the magnetic topology. Please note the different color-bar styles used in the two subplots for better representation.

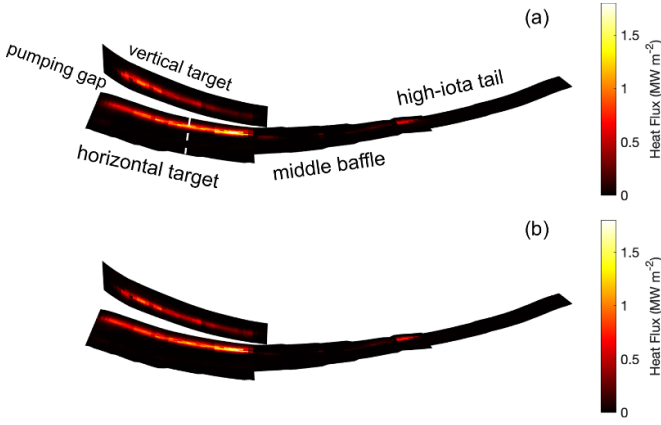


**Figure 7.** Comparisons of experimental and simulated heat flux profiles on the divertor target at the stellarator-symmetric toroidal position with divertor Langmuir probes as shown in figures 2 and 8. The dotted background curves are heat flux profiles on different divertor modules measured by infrared cameras. The black solid curve is the averaged heat flux profile on different divertor modules.

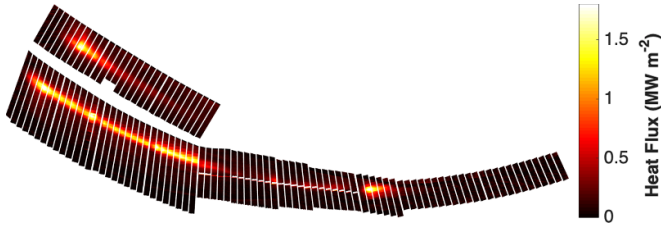
The magnetic topology changes induced by high beta effects have significant influences on heat and particle fluxes on divertor targets. Figure 13 depicts the divertor heat flux

distribution simulated by EMC3-EIRENE with the density scan in the vacuum field case and the central beta 5% case with  $p \propto (1 - s)^3$ . It is clear that the heat flux with beta effects

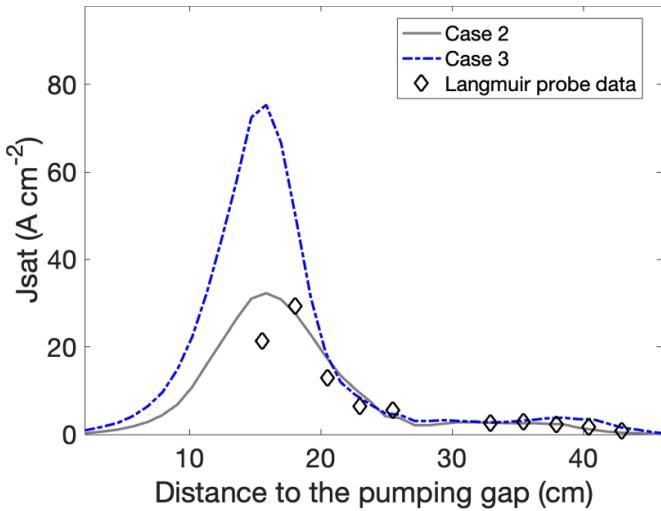




**Figure 8.** The heat flux distributions on the divertor target in (a) case 2 and (b) case 3 simulated by EMC3-EIRENE combined with HINT. The white dashed line in (a) marks the position of profiles shown in figure 7.

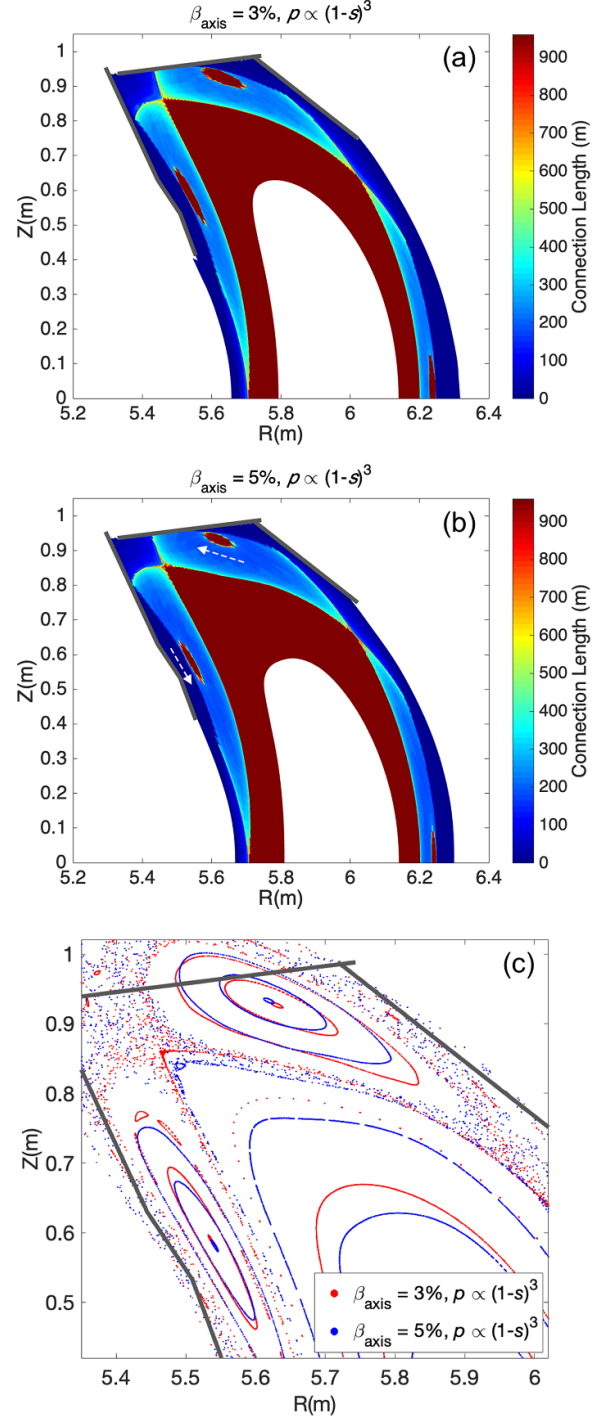


**Figure 9.** The average heat flux distribution measured by infrared cameras on divertor modules.



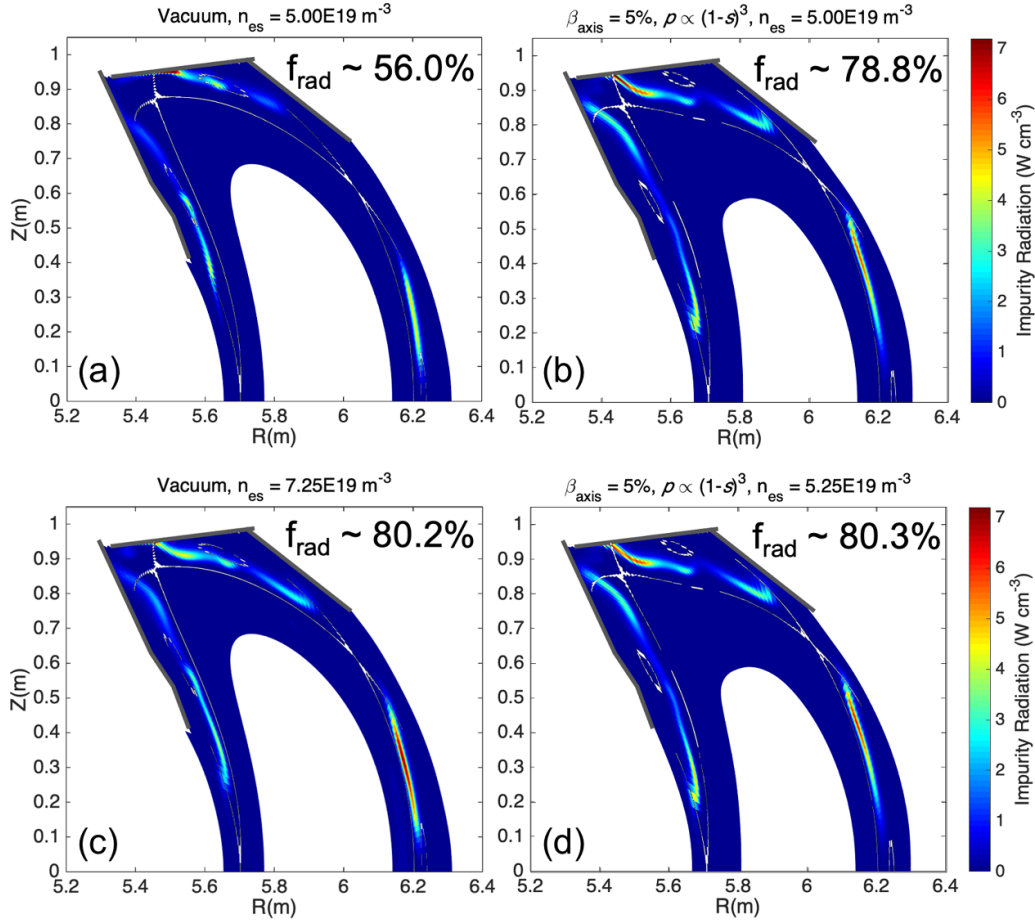
**Figure 10.** Comparisons of parallel ion saturation currents between EMC3-EIRENE calculations and experimental data measured by target probe arrays.

is distributed more evenly along the toroidal direction on the strike line at the vertical target. Combined with figure 11, it can be seen that in high beta plasmas, the strike line on horizontal divertor targets moves towards the pumping gap as a result of the modification of the magnetic island structure. Additionally, the divertor heat flux is almost always reduced with increases in the separatrix density due to the power dissipation.



**Figure 11.** The connection length distributions of magnetic field lines with the central plasma beta of (a) 3% and (b) 5%. The white arrow in (b) marks a shift in the magnetic island core in the poloidal direction, caused by beta effects. The subplot (c) illustrates the Poincaré plot of the magnetic topology for the above two cases. The central plasma beta of 3% and 5% scenarios are represented by red and blue colors respectively.

However, in some specific positions, such as the area surrounded by a dashed white circle, the heat flux firstly increases and then decreases. This is because the plasma cross-field transport ( $\sim \chi n \nabla T$ ), which is influenced by the synergistic effect of density  $n$  and temperature gradient  $\nabla T$  changes, is modified



**Figure 12.** The simulated impurity radiation power distributions at the bean shape cross-section in the vacuum case and the central beta 5% case with  $p \propto (1-s)^3$ .  $f_{\text{rad}}$  is the percentage of the impurity radiation power to the total input power. The white curves indicate the separatrix and magnetic island core locations.

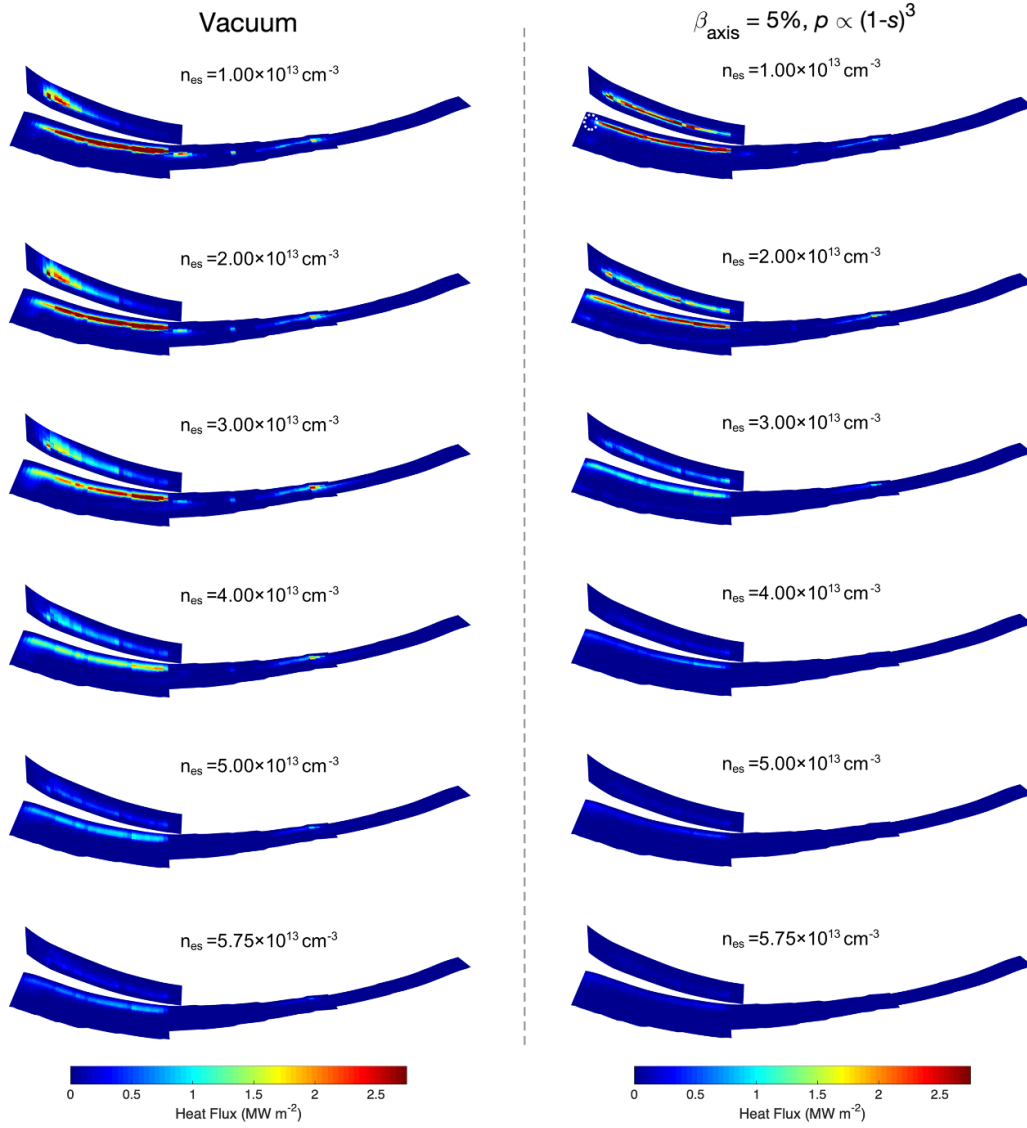
as the density increases. Figure 14 provides an example of how the beta effect modifies the divertor particle flux pattern. The shape of the strike lines and the flux amplitude show a marked difference with the same separatrix density in the two scenarios.

Figure 15(a) shows the dependence of the recycling flux on the separatrix density in the different modeling cases. As can be seen, the separatrix density corresponding to the peak recycling flux is reduced with an increase in the plasma beta. It means the threshold separatrix density for accessing the power detachment is reduced in higher beta plasmas. Before the recycling flux starts to decrease, compared with the vacuum field case, the increased radial transport caused by the magnetic topology changes in higher beta cases leads to more divertor particle flux and concomitant impurity particle source, thus resulting in a higher power dissipation in the scrape-off layer (SOL). Not only this, the changes of the impurity transport induced by the magnetic topology modification also contribute to the increases of the impurity radiation power. An increase in the plasma beta leads to an enhancement of edge stochasticization [12], facilitating the deeper penetration of impurities in the magnetic island region. Figure 15(b) depicts the recycling flux as a function of the total radiation power in different beta strength plasmas. The recycling flux drops

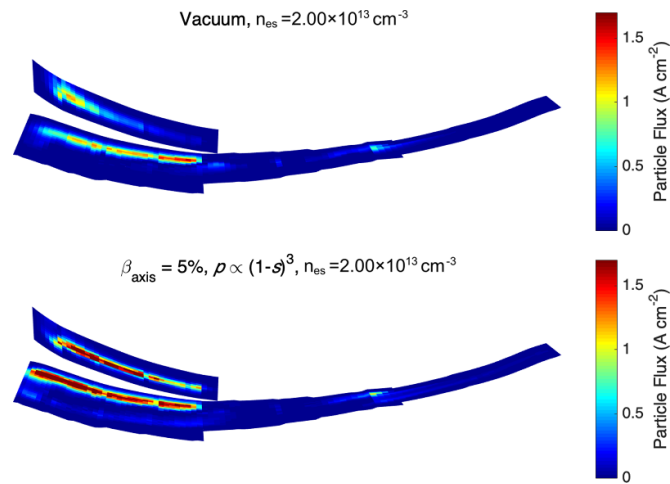
almost linearly when the downstream  $T$  is below  $\sim 4$  eV, which is in line with the result in [45]. Further analysis of this phenomenon can be found in this reference.

### 3.2. Plasma pressure profile

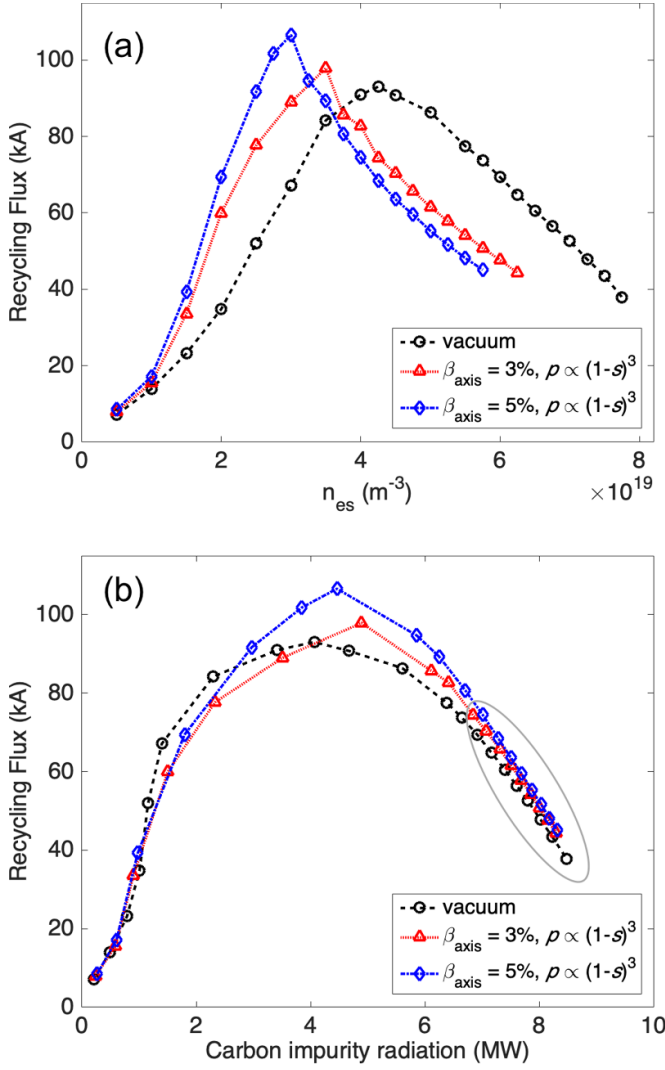
Via simulations, it is found that different form of the plasma pressure profile has essential effects on the magnetic field distributions. So far, the plasma pressure profile cannot be confirmed in high beta plasmas due to lacks of reference discharges on W7-X. In this sub-section, another typical profile form  $p \propto (1-s)^1$  is studied to assess the influence of the different pressure profile on the edge plasma transport. The different pressure profiles with same plasma central beta mean a change of the volume-averaged beta. So, two cases using this pressure profile form with the central beta of 5% and 2.5% are studied. The latter case ( $\beta_{\text{axis}} = 2.5\%$ ) has an almost same volume-averaged beta with the case of  $\beta_{\text{axis}} = 5\%$  with  $p \propto (1-s)^3$ . Figure 16 illustrates the connection length distribution and the Poincaré plot of field lines in above scenarios. Compared with figure 11(b), the magnetic island structure is significantly modified due to the initial drive of the different pressure profiles. It can be seen that both the separatrix shape and the magnetic island structure are changed visibly.



**Figure 13.** The heat flux distributions on the divertor target simulated by EMC3-EIRENE with the separatrix density scan in the vacuum field scenario (left) and the central beta 5% case with  $p \propto (1-s)^3$  (right).



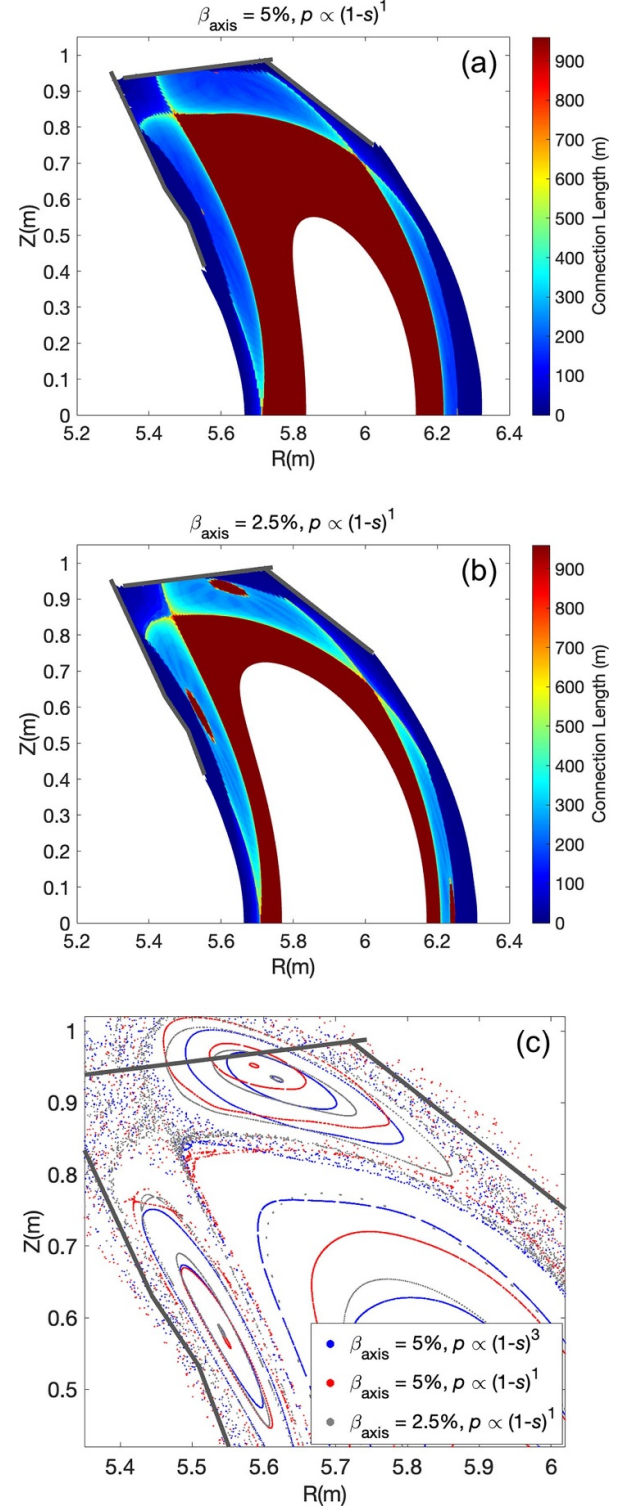
**Figure 14.** The simulated particle flux distributions with  $n_{es} = 2.0 \times 10^{13} \text{ cm}^{-3}$  on the divertor target in the vacuum field case (up) and the central beta 5% case with  $p \propto (1-s)^3$  (down).



**Figure 15.** The recycling flux as a function of (a) the separatrix density and (b) the impurity radiation power simulated by EMC3-EIRENE combined with HINT. In the modeling cases within the gray elliptic in (b), the downstream temperature is approximately below  $\sim 4$  eV.

Figure 17 shows an example of the heat flux distribution on the divertor target by using the new pressure profile in simulations. Compared to figure 13, an obvious difference is that there is a secondary strike line appeared on the horizontal target. To understand the physical mechanism behind, the connection length distributions near the target at a toroidal position of  $\varphi = -4.5^\circ$  are illustrated in figure 18. The toroidal position marked as a gray line in figure 17. The magnetic island structure is changed due to plasma responses in high beta plasmas. As can be seen, for the case with the pressure profile  $p \propto (1-s)^1$ , the long connection length region along the separatrix on the right side of the magnetic island near the target touches the horizontal divertor target, thus leading to the secondary strike line mainly by the parallel plasma transport.

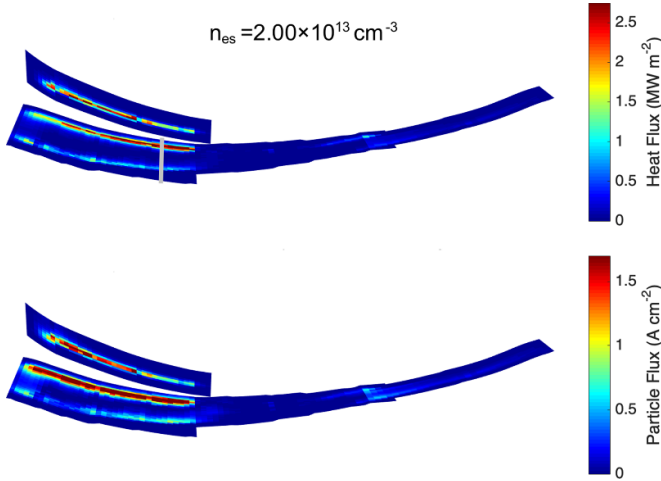
The non-linear recycling flux behavior is also studied by a series of EMC3-EIRENE simulations with the separatrix density scan. As shown in figure 19, the threshold separatrix density for accessing the power detachment obviously changes



**Figure 16.** The connection length distributions of magnetic field lines at the bean shape cross-section in the central beta (a) 5% and (b) 2.5% cases with  $p \propto (1-s)^1$ . The subplot (c) illustrates the Poincaré plot of the magnetic field lines for the previously mentioned cases.

with the pressure profile modification with a fixed plasma volume-averaged beta. However, with a fixed central beta, the pressure profile form shows a much weak effect on detachment threshold separatrix density in the studied cases. Comparing



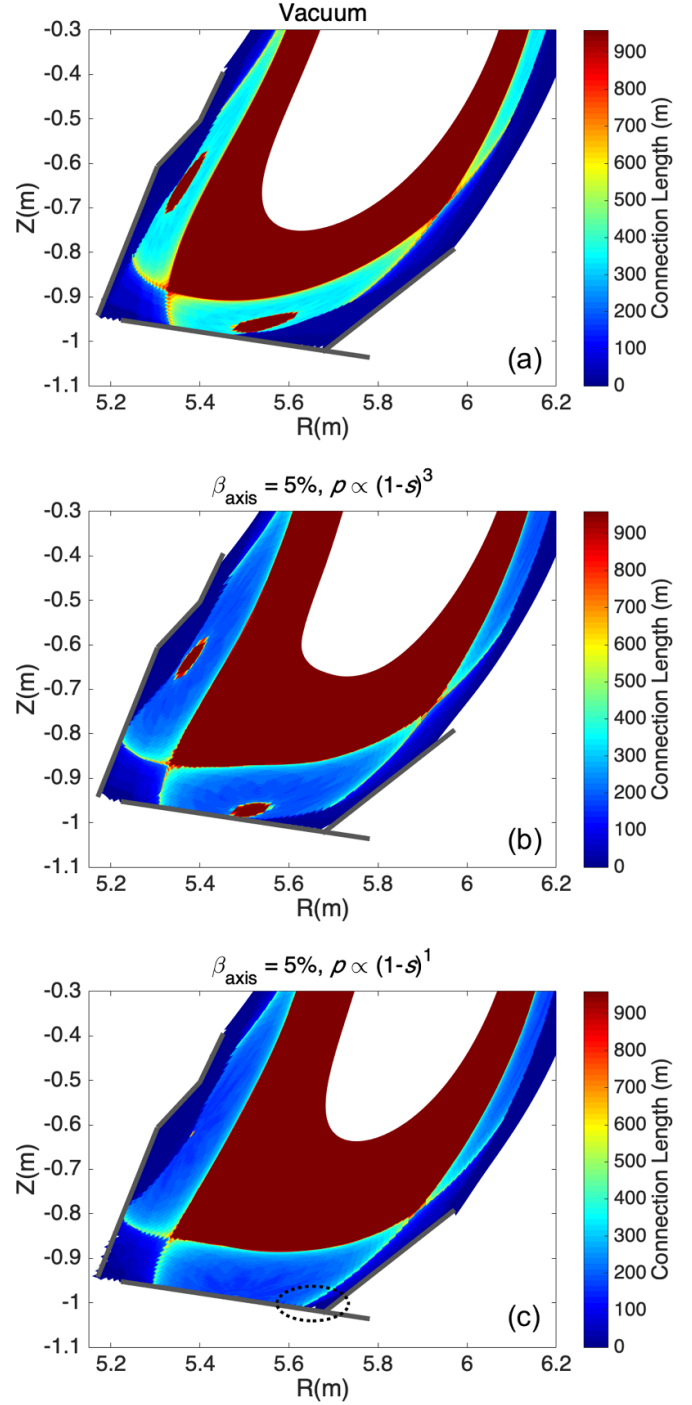


**Figure 17.** The heat flux and the particle flux distributions on the divertor target simulated by EMC3-EIRENE in the central beta 5% case with  $p \propto (1-s)^1$ . Here, the simulation uses  $n_{es} = 2.0 \times 10^{13} \text{ cm}^{-3}$  as an example. The gray line marks the toroidal position for figure 18.

the two scenarios with  $\beta_{vol} \sim 1.25\%$ , the recycling fluxes are different while plasmas start into the power detachment state. In detached plasmas, the case with the pressure profile  $p \propto (1-s)^3$  has a less recycling flux, corresponding to less carbon sources released by divertor targets, but it has higher radiation power as shown in figure 19(b). The reason is that the radiation front moves towards the plasma core region in detached plasmas. A large number of impurity particles enter the magnetic island region, thus amplifying the influence of the island structure changes on the global impurity behavior.

### 3.3. Toroidal plasma current amplitude

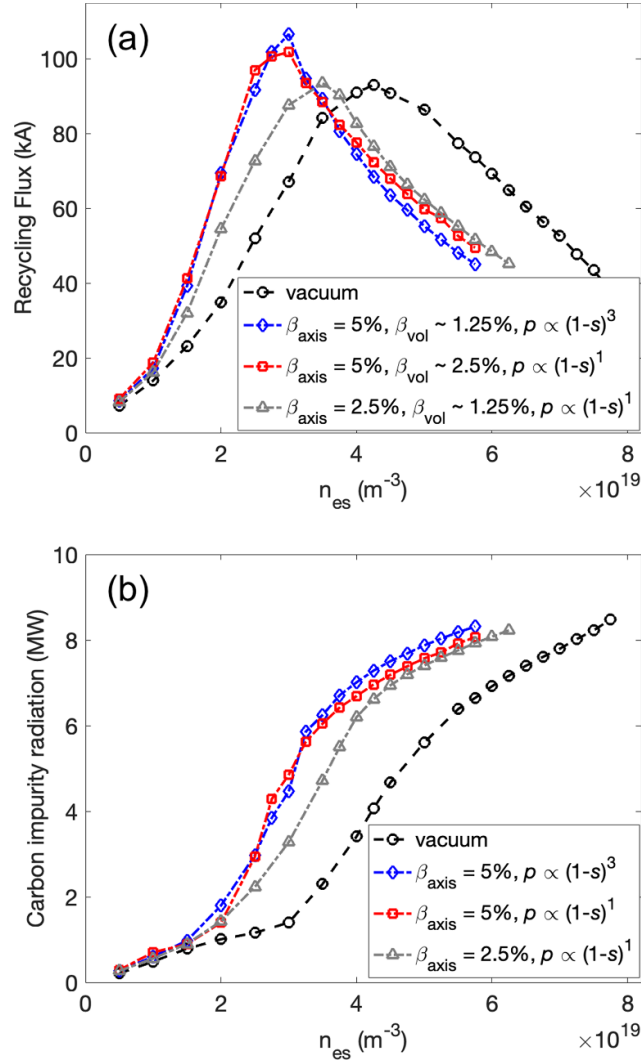
This sub-section will pay attention to the synergy effect of the plasma beta and toroidal plasma currents on the edge plasma transport. Although the magnetic configurations on W7-X are developed based on an optimization process, there are still toroidal plasma currents appearing in experiments, because of the intrinsic bootstrap current, the additional externally driven current, or the transiently appearing plasma shielding current [59]. Here, the toroidal plasma current is quite different from the Pfirsch–Schlüter current driven by the pressure gradient in beta effects. Similar to a previous work [12], a toroidal net plasma current amplitude of 5 kA with a profile of  $I \propto (1-s)^2$  is assumed in the following qualitative study. Figure 20 shows the simulated connection length distribution of field lines with positive toroidal currents in a central beta of 5% plasma at the bean shape cross-section. The direction of the toroidal current is clockwise from the top view. Compared to figure 11(b), a positive toroidal plasma current increases the edge iota, thus moving the magnetic island chain towards the magnetic axis because of the positive shear at the plasma edge. The shrink of the separatrix leads to the strike line moving away from the pumping gap on the divertor targets, which is consistent with the experimental observations [59].



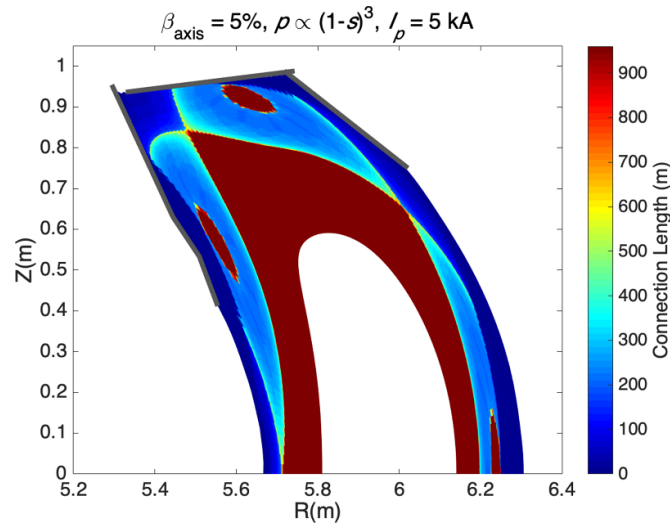
**Figure 18.** The connection length distributions of magnetic field lines near the divertor target at a toroidal position of  $\varphi = -4.5^\circ$  in the vacuum field case and the central beta 5% cases with different pressure profiles. The toroidal position is marked in figure 17. The area of interest is marked by a dotted ellipse in (c).

The impurity radiation power and the recycling flux as a function of the separatrix density are illustrated in figure 21 based on EMC3-EIRENE modeling. It seems that the influence of the toroidal plasma current on the edge plasma is not as serious as that of beta effects. The reason is that unlike beta effects, the magnetic topology changes induced by the toroidal current does not produce many harmonics with high

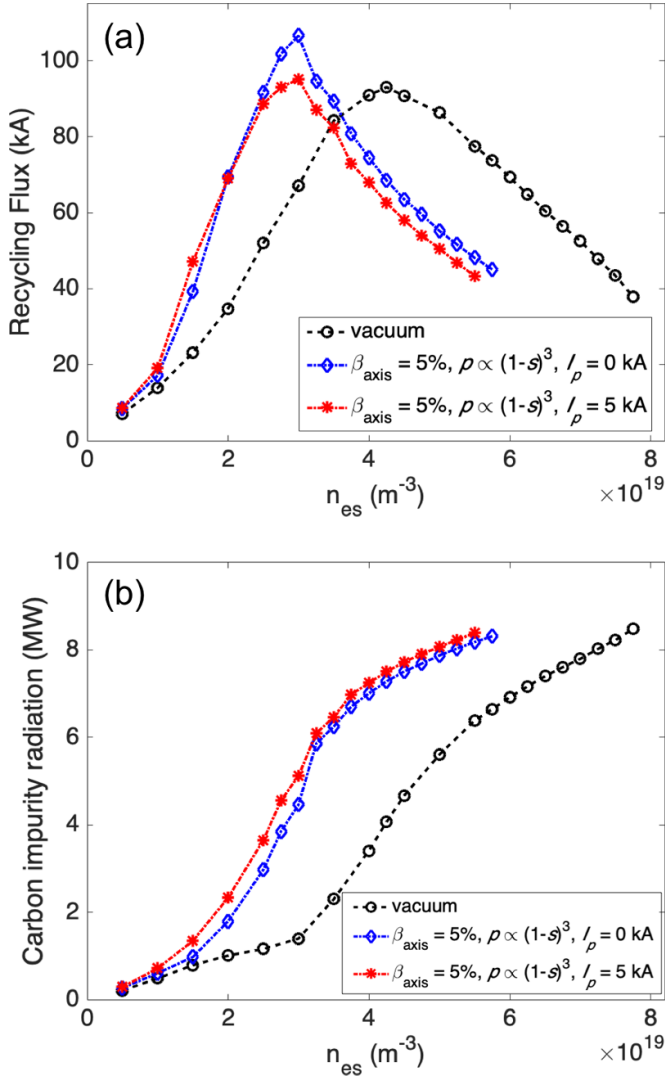




**Figure 19.** (a) The recycling flux and (b) the impurity radiation power as a function of the separatrix density in different pressure profile scenarios. The cases marked by blue and gray lines have the almost same volume beta. The cases marked by blue and red lines have the same central beta.



**Figure 20.** The connection length distributions of magnetic field lines in the central beta 5% case with  $p \propto (1-s)^3$  and a positive toroidal plasma current of 5 kA.



**Figure 21.** (a) The recycling flux and (b) the impurity radiation power as a function of the separatrix density in the vacuum field case and the central beta 5% case with different toroidal plasma currents.

toroidal mode numbers. The influence of the toroidal current on the radial transport is weaker than that of the beta effects. The toroidal current amplitude of 5 kA is also not large enough to induce a significant difference. It is also worth mentioned that the peak recycling flux is reduced with higher toroidal plasma current due to the modification of magnetic field distributions.

#### 4. Conclusion and discussion

The island divertor transport with finite beta effects has been studied in the standard configuration on W7-X by utilizing EMC3-EIRENE combined with the HINT code. In simulations, the HINT calculations provide the 3D equilibrium field with finite beta effects to EMC3-EIRENE. The grid generation for EMC3-EIRENE on W7-X has been improved to be capable of using HINT results directly. To validate the modeling strategy, a representative standard configuration shot (ID #20180814034) is studied in detail. By adjusting the

input free parameters in the modeling, an agreement can be obtained between modeling results and experimental data at both upstream and downstream positions. The magnetic island structure is clearly reflected in the edge plasma, highlighting the importance of considering both the beta effect and toroidal plasma currents in accurate simulations of edge plasma transports for high-performance plasmas. The result also indicates that multiple diagnostics at the plasma edge are needed to improve input free parameters of EMC3-EIRENE simulations, because of the complex 3D effects in stellarator plasmas. The differences between modeling and experiments may be caused by HINT abilities, the assumed uniform cross-field transport coefficient, the  $E \times B$  drift effect, the error magnetic field, and so on. The current version of the EMC3-EIRENE calculations does not take into account the existence of error fields, and the self-treatment of drift effects [46].

To support future W7-X experiments, the influence of plasma beta effects on the power dissipation in high heating power plasmas with the standard configuration has been studied after validation of the modeling strategy. The results show that the threshold separatrix density for accessing the power detachment is reduced in higher beta plasmas. This means the detachment may be easier to be achieved than expected in high beta plasmas. Such threshold separatrix density of the detachment is also affected by the pressure profile form in the same volume-averaged beta plasmas. The essential reason is the magnetic topology changes caused by beta effects, including the modified magnetic island structure and enhanced edge stochasticization. It should be mentioned that high beta plasmas are usually achieved by increasing the heating power in experiments. The heating power itself also has an effect on accessing the detachment. The synergistic influences of beta effects and the heating power on the threshold separatrix density for the detachment should be further studied by experiments combined with EMC3-EIRENE modeling.

For the divertor flux, the magnetic topology changes induced by high beta effects have significant influences on heat and particle fluxes on divertor targets. The different pressure profiles with the same central beta also result in modified heat flux patterns on divertor targets. The strike line on horizontal divertor targets moves towards the pumping gap with an increase in the plasma beta, while it moves away from the pumping gap with the positive toroidal plasma current. This should be highlighted in the preparation of future high performance experiments to avoid potential operational risks. Additionally, the movement of the strike line, caused by toroidal plasma currents, has been found to modify the divertor neutral pressure in past experiments. The sensitivity of the neutral pressure to the strike line location decreases as the radiation front moves further away from targets at high radiation levels [45]. Here, it is also expected that the movement of the strike line caused by beta effects will have an impact on the divertor neutral pressure control and pumping effects. Moreover, compared to the vacuum field case, impurity transport behaviors with finite beta effects are significantly changed in the magnetic island region. It can be inferred that the plasma beta effects should have an influence on the access of detached plasmas by active impurity seeding. These topics should be




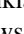


further studied with support from high beta experiments in the future.

## Acknowledgments

This work has been carried out within the framework of the EUROfusion Consortium, funded by the European Union via the Euratom Research and Training Programme (Grant Agreement No. 101052200—EUROfusion). Views and opinions expressed are however those of the author(s) only and do not necessarily reflect those of the European Union or the European Commission. Neither the European Union nor the European Commission can be held responsible for them.

The authors gratefully acknowledge the computing time granted by the JARA-HPC Vergabegremium and VSR commission on the supercomputer JURECA [60] at Forschungszentrum Jülich.

## ORCID iDs

S. Xu  <https://orcid.org/0000-0002-0033-3468>  
 A. Knieps  <https://orcid.org/0000-0003-0083-7188>  
 S. Zhou  <https://orcid.org/0000-0002-1407-0574>  
 Y. Feng  <https://orcid.org/0000-0002-3846-4279>  
 Y. Suzuki  <https://orcid.org/0000-0001-7618-6305>  
 M. Jia  <https://orcid.org/0000-0002-1672-9782>  
 J. Geiger  <https://orcid.org/0000-0003-4268-7480>  
 A. Dinklage  <https://orcid.org/0000-0002-5815-8463>  
 P. Drews  <https://orcid.org/0000-0002-6567-1601>  
 M. Jakubowski  <https://orcid.org/0000-0002-6557-3497>  
 Y. Gao  <https://orcid.org/0000-0001-8576-0970>  
 A. Langenberg  <https://orcid.org/0000-0002-2107-5488>  
 N. Pablant  <https://orcid.org/0000-0001-6617-8459>  
 S. Brezinsek  <https://orcid.org/0000-0002-7213-3326>

## References

- [1] Klinger T. et al 2017 *Plasma Phys. Control. Fusion* **59** 014018
- [2] Pedersen T.S. et al 2017 *Phys. Plasmas* **24** 055503
- [3] Wolf R.C. et al 2017 *Nucl. Fusion* **57** 102020
- [4] Klinger T. 2016 *Magnetic Fusion Energy: From Experiments to Power Plants* ed G. Neilson (Cambridge: Woodhead Publishing)
- [5] König R. et al 2002 *Plasma Phys. Control. Fusion* **44** 2365
- [6] Pedersen T.S. et al 2022 *Nucl. Fusion* **62** 042022
- [7] Klinger T. et al 2019 *Nucl. Fusion* **59** 112004
- [8] Suzuki Y. and Geiger J. 2016 *Plasma Phys. Control. Fusion* **58** 064004
- [9] Liang Y. et al 2017 *Nucl. Fusion* **57** 066049
- [10] Suzuki Y. et al 2020 *Plasma Phys. Control. Fusion* **62** 104001
- [11] Knieps A. et al 2022 *Nucl. Fusion* **62** 026011
- [12] Zhou S. et al 2022 *Nucl. Fusion* **62** 106002
- [13] Evans T. et al 2006 *Nat. Phys.* **2** 419–23
- [14] Jakubowski M.W. et al 2006 *Phys. Rev. Lett.* **96** 035004
- [15] Liang Y. et al 2007 *Phys. Rev. Lett.* **98** 265004
- [16] Liang Y. et al 2013 *Phys. Rev. Lett.* **110** 235002
- [17] Kobayashi M. et al 2015 *Nucl. Fusion* **55** 104021
- [18] Jia M. et al 2018 *Nucl. Fusion* **58** 046015
- [19] Jia M. et al 2021 *Nucl. Fusion* **61** 106023
- [20] Kobayashi M. et al 2019 *Nucl. Fusion* **59** 096009
- [21] Pedersen T.S. et al 2019 *Nucl. Fusion* **59** 096014
- [22] Xu S. et al 2018 *Nucl. Fusion* **58** 106008
- [23] Xu S. et al 2020 *Nucl. Fusion* **60** 056006
- [24] Wang H. et al 2021 *Plasma Sci. Technol.* **23** 125103
- [25] Feng Y. et al 1999 *J. Nucl. Mater.* **266–269** 812–8
- [26] Feng Y. et al 2014 *Contrib. Plasma Phys.* **54** 426–31
- [27] Reiter D., Baelmans M. and Börner P. 2005 *Fusion Sci. Technol.* **47** 172–86
- [28] EIRENE (available at: <http://eirene.de>)
- [29] Suzuki Y., Nakajima N., Watanabe K., Nakamura Y. and Hayashi T. 2006 *Nucl. Fusion* **46** L19
- [30] Suzuki Y. et al 2017 *Plasma Phys. Control. Fusion* **59** 054008
- [31] Rack M., Reiter D., Hasenbeck F., Feng Y., Börner P., Weger A.-C. and Cosfeld J. 2017 *Nucl. Fusion* **57** 056011
- [32] Kobayashi M. et al 2013 *Nucl. Fusion* **53** 093032
- [33] Dai S., Kobayashi M., Kawamura G., Morita S., Zhang H.M., Oishi T., Feng Y., Wang D.Z. and Suzuki Y. 2016 *Nucl. Fusion* **56** 066005
- [34] Pandya S. et al 2016 *Nucl. Fusion* **56** 046002
- [35] Feng Y., Sardei F., Grigull P., McCormick K., Kisslinger J., Reiter D. and Igutkhanov Y. 2002 *Plasma Phys. Control. Fusion* **44** 611–25
- [36] Feng Y., Sardei F., Kisslinger J., Grigull P., McCormick K. and Reiter D. 2004 *Contrib. Plasma Phys.* **44** 57–69
- [37] Feng Y. et al 2005 *Nucl. Fusion* **45** 89–95
- [38] Feng Y., Sardei F., Grigull P., McCormick K., Kisslinger J. and Reiter D. 2006 *Nucl. Fusion* **46** 807–19
- [39] Sharma D., Feng Y., Sardei F. and Reiter D. 2005 *Nucl. Fusion* **45** 825–36
- [40] Feng Y., Beidler C.D., Geiger J., Helander P., Hölbe H., Maassberg H., Turkin Y. and Reiter D. 2016 *Nucl. Fusion* **56** 126011
- [41] Feng Y., Frerichs H., Kobayashi M. and Reiter D. 2017 *Plasma Phys. Control. Fusion* **59** 034006
- [42] Winters V. et al 2021 *Plasma Phys. Control. Fusion* **63** 045016
- [43] Effenberg F. et al 2017 *Nucl. Fusion* **57** 036021
- [44] Effenberg F. et al 2019 *Nucl. Fusion* **59** 106020
- [45] Feng Y. et al 2021 *Nucl. Fusion* **61** 086012
- [46] Feng Y. et al 2021 *Nucl. Fusion* **61** 106018
- [47] Geiger J., Beidler C.D., Feng Y., Maaßberg H., Marushchenko N.B. and Turkin Y. 2015 *Plasma Phys. Control. Fusion* **57** 014004
- [48] Zhang D. et al 2010 *Rev. Sci. Instrum.* **81** 10E134
- [49] Zhang D. et al 2019 *Phys. Rev. Lett.* **123** 025002
- [50] Pasch E., Beurskens M.N.A., Bozhnikov S.A., Fuchert G., Knauer J. and Wolf R.C. 2016 *Rev. Sci. Instrum.* **87** 11E729
- [51] Rudischhauser L., Endler M., Höfel U., Hammond K.C., Kallmeyer J.P. and Blackwell B.D. 2020 *Rev. Sci. Instrum.* **91** 063505
- [52] Jakubowski M. et al 2018 *Rev. Sci. Instrum.* **89** 10E116
- [53] Gao Y., Jakubowski M.W., Drewelow P., Pisano F., Puig Sitjes A., Niemann H., Ali A. and Cannas B. 2019 *Nucl. Fusion* **59** 066007
- [54] Kring J., Pablant N., Langenberg A., Rice J., Delgado-Aparicio L., Maurer D., Traverso P., Bitter M., Hill K. and Reinke M. 2018 *Rev. Sci. Instrum.* **89** 10F107
- [55] Feng Y., Lunt T., Sardei F. and Zha X. 2013 *Comput. Phys. Commun.* **184** 1555–61
- [56] Kotov V., Reiter D., Pitts R.A., Jachmich S., Huber A. and Coster D.P. 2008 *Plasma Phys. Control. Fusion* **50** 105012
- [57] Jakubowski M. et al 2021 *Nucl. Fusion* **61** 106003
- [58] Schmitz O. et al (The W7-X Team) 2021 *Nucl. Fusion* **61** 016026
- [59] Gao Y. et al 2019 *Nucl. Fusion* **59** 106015
- [60] Krause D. and Thörnig P. (Jülich Supercomputer Centre) 2018 *J. Large-Scale Res. Facil.* **4** A132